

# Enhancing Spin-Orbit Torque by Strong Interfacial Scattering From Ultrathin Insertion Layers

Lijun Zhu,<sup>1,\*</sup> Lujun Zhu,<sup>2</sup> Shengjie Shi,<sup>1</sup> Manling Sui,<sup>3</sup> D.C. Ralph,<sup>1,4</sup> and R.A. Buhrman<sup>1</sup>

<sup>1</sup>Cornell University, Ithaca, New York 14850, USA

<sup>2</sup>College of Physics and Information Technology, Shaanxi Normal University, Xi'an 710062, China

<sup>3</sup>Institute of Microstructure and Property of Advanced Materials, Beijing University of Technology, Beijing 100124, China

<sup>4</sup>Kavli Institute at Cornell, Ithaca, New York 14853, USA

(Received 1 March 2019; published 7 June 2019)

Increasing dampinglike spin-orbit torque (SOT) is of fundamental importance for enabling new research into spintronics phenomena and also technologically urgent for advancing low-power spin-torque memory, logic, and oscillator devices. Here, we demonstrate that enhancing interfacial scattering by inserting ultrathin layers within spin Hall metals with intrinsic or side-jump mechanisms can significantly enhance the spin Hall ratio. The dampinglike SOT is enhanced by a factor of 2 via submonolayer Hf insertion, as evidenced by both harmonic response measurements and current-induced switching of in-plane magnetized magnetic memory devices with the record low critical switching current of approximately 73  $\mu\text{A}$  (switching current density of approximately  $3.6 \times 10^6 \text{ A/cm}^2$ ). This work demonstrates a very effective strategy for maximizing dampinglike SOT for low-power spin-torque devices.

DOI: 10.1103/PhysRevApplied.11.061004

## I. INTRODUCTION

Spin-orbit torques (SOTs) generated by the spin Hall effect (SHE) can efficiently switch thin-film nanomagnet devices [1–4], excite magnetization oscillations [5], and drive skyrmion and chiral domain-wall displacement [6–8]. Increasing SOT efficiencies is of great importance for enabling new research into spintronics phenomena [1–9] and for advancing technological applications of SOTs [10–13]. Of particular interest in this effort is to develop heavy metals (HMs) that can simultaneously provide a large dampinglike SOT efficiency per current density ( $\xi_{\text{DL}}^j$ ), easy growth, good chemical and thermal stability, and the capability to be readily integrated into complex experimental configurations and/or into manufacturing processes. A good representative of such HMs is Pt, which has giant spin Hall conductivity ( $\sigma_{\text{SH}}$ ) arising from the Berry curvature of its band structure [14,15]. For the SHE,  $\xi_{\text{DL}}^j \equiv (2e/\hbar)T_{\text{int}}\sigma_{\text{SH}}\rho_{xx}$ , with  $e$ ,  $\hbar$ ,  $\rho_{xx}$ , and  $T_{\text{int}}$  being the elementary charge, the reduced Planck's constant, the HM resistivity, and the spin transparency of the HM-ferromagnet (FM) interface [9].  $\xi_{\text{DL}}^j$  for Pt/FM systems is approximately 0.08 where  $\rho_{xx} = 20 \mu\Omega \text{ cm}$  [16]. Recently, impurity scattering has been demonstrated to increase  $\xi_{\text{DL}}^j$  via enhancing  $\rho_{xx}$  [17–20]. However, in all the previous work the increase of  $\xi_{\text{DL}}^j$  was limited (e.g.,

to  $\xi_{\text{DL}}^j = 0.12 - 0.3$  for 4-nm Pt alloys) due to a fast decrease in  $\sigma_{\text{SH}}$  with doping level [19] and/or only a weak enhancement of  $\rho_{xx}$  [17,18]. Exploring new enhancement strategies that can better optimize the trade-offs between  $\rho_{xx}$  and  $T_{\text{int}}\sigma_{\text{SH}}$  is of both fundamental interest and technological urgency (e.g., for low-power magnetic memories, logic, and oscillators).

In this work, we report that introducing strong interfacial electron scattering via the insertion of submonolayers of Hf into Pt can enhance  $\rho_{xx}$  of an approximate 4-nm Pt layer by a factor of 5, which beneficially results in 100% enhancement of  $\xi_{\text{DL}}^j$  (up to 0.37). The increase in  $\xi_{\text{DL}}^j$  by the ultrathin insertion layers is approximately twice as effective as a uniform alloying of Hf into Pt. This giant enhancement of  $\xi_{\text{DL}}^j$  by Hf insertion layers is reaffirmed by the deterministic switching of in-plane magnetic tunnel junctions (MTJs) at a low zero-temperature critical current of approximately 73  $\mu\text{A}$  (current density of approximately  $3.6 \times 10^6 \text{ A/cm}^2$ ) as determined from ramp-rate measurements.

## II. RESULTS AND DISCUSSIONS

### A. Enhancing resistivity by interfacial scattering

The main idea of this work is schematically shown in Fig. 1. In a single metallic layer of Pt that is not too thin, e.g., 4 nm as typically used for spin-torque magnetic random-access memories (MRAMs) [10], the resistivity

\*lz442@cornell.edu

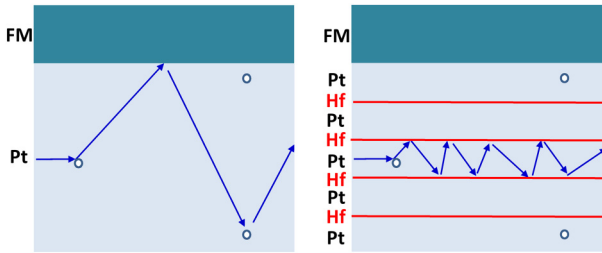


FIG. 1. Schematic depiction of interfacial scattering enhancement of the resistivity.

arises mainly from the electron scattering by impurities and thermal phonons inside the Pt layer and is hence relatively low, e.g.,  $20\text{--}50 \mu\Omega \text{ cm}$  at room temperature [16–21]. In contrast, if we “dice” the same Pt layer into several layers by inserting multiple ultrathin Hf layers during the deposition process, the new Pt/Hf interfaces should introduce strong additional interfacial scattering of electrons and hence greatly enhance the averaged  $\rho_{xx}$ . The Pt crystal structure between the interfaces can be disrupted less than would be the case for uniform alloying with Hf [19], thereby better preserving the large intrinsic  $\sigma_{SH}$  of Pt and better enhancing  $\xi_{DL}^j$ .

We sputter-deposit magnetic stacks of Ta(1.0 nm)/[Pt( $d$  nm)/Hf(0.2 nm)] $_n$ /Pt( $d$  nm)/Co( $t$  nm)/MgO(2.0 nm)/Ta(1.5 nm) with  $d = 0.4, 0.5, 0.6, 0.75, 1, 1.5, 2$ , and 4 nm. Here  $n$  ( $\leq 7$ ) is chosen to be the integer that can make the total Pt thickness closest to 4 nm under the constraint that the total Hf thickness is no more than 1.4 nm (note that the spin diffusion length  $\lambda_s$  of the amorphous Hf is approximately 1 nm [22]). For the perpendicular magnetic anisotropy (PMA) samples, the Co thickness  $t$  is 0.83 nm for  $d \geq 1$  and 0.63 nm for  $d \leq 0.75$  nm; for in-plane magnetic anisotropy (IMA) samples,  $t$  is 1.3 nm for  $d \geq 1$  and 0.93 nm for  $d \leq 0.75$  nm. The samples are further patterned into  $5 \times 60 \mu\text{m}^2$  Hall bars [see Fig. 2(a)] for resistivity and SOT measurements (see Supplemental Materials [23]).

As shown in Fig. 2(b), the average resistivity of the [Pt( $d$  nm)/Hf(0.2 nm)] $_n$ /Pt( $d$  nm) multilayer is increased from  $37 \mu\Omega \text{ cm}$  for  $d = 4$  nm (pure Pt) to  $191 \mu\Omega \text{ cm}$  for  $d = 0.4$  ([Pt(0.4 nm)/Hf(0.2 nm)] $_7$ /Pt(0.4 nm)). Compared to that achieved by alloying or impurity doping ( $83 \mu\Omega \text{ cm}$  for Au $_{0.25}$ Pt $_{0.75}$  and  $110 \mu\Omega \text{ cm}$  for Pt $_{0.85}$ Hf $_{0.15}$ ) [18–21], this is a remarkable resistivity enhancement despite the fact that the 0.2-nm Hf insertions are too thin to be distinguishable by either x-ray diffraction and/or reflectivity or scanning tunneling electron microscopy (STEM) and electron dispersive spectroscopy (EDS) measurements (see Figs. S1–S3 within the Supplementary Material [23]).

## B. Magnifying spin torque by interfacial scattering

Figure 2(c) summarizes the values of  $\xi_{DL}^j$  determined from harmonic response measurements [24,25] on both

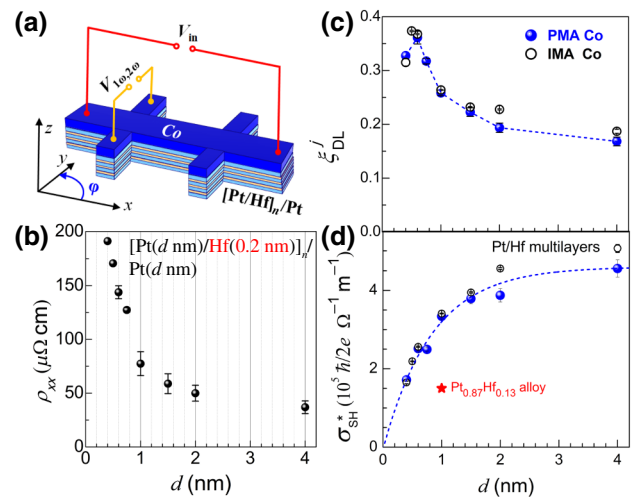


FIG. 2. (a) Geometry and coordinates for the SOT measurements; (b) measured resistivity of [Pt( $d$  nm)/Hf(0.2 nm)] $_n$ /Pt( $d$  nm) multilayers as a function of the “slice” thickness  $d$  of the individual Pt layers; (c) the dampinglike spin-torque efficiency ( $\xi_{DL}^j$ ); and (d) the apparent spin Hall conductivity ( $\sigma_{SH}^*$ ) determined from harmonic-response measurements for both PMA (blue dots) and IMA (black circles) samples plotted as a function of  $d$ . The dashed lines are guides to the eye. The red star denotes the value of  $\sigma_{SH}^*$  for 4 nm of a spatially uniform Pt $_{0.87}$ Hf $_{0.13}$  alloy [19].

the PMA and IMA multilayers as a function of  $d$ , with good agreement between the two types of measurements (see Figs. S4 and S5 within the Supplementary Material [23]). For both the PMA and IMA samples,  $\xi_{DL}^j$  increases quickly from  $0.17 \pm 0.01$  at  $d = 4$  nm (pure Pt) to a peak at  $d = 0.6$  nm and then drops slightly as  $d$  increases further to 0.4 nm. The peak value of  $\xi_{DL}^j = 0.37 \pm 0.01$  for  $d = 0.6$  nm (i.e., [Pt(0.6 nm)/Hf(0.2 nm)] $_5$ /Pt(0.6 nm) multilayers) is significantly higher than the values reported for Pt $_{0.85}$ Hf $_{0.15}$  ( $\xi_{DL}^j \approx 0.15$ ) [19], Au $_{0.25}$ Pt $_{0.75}$  ( $\xi_{DL}^j \approx 0.30$ ) [18],  $\beta$ -W ( $\xi_{DL}^j \approx 0.2 - 0.3$ ) [13,26] and  $\beta$ -Ta ( $\xi_{DL}^j \approx 0.12$ ) [3]. We attribute the increase of  $\xi_{DL}^j$  for Pt/Hf multilayers to the enhanced resistivity from interface scattering [see Fig. 2(b)]. Based on the comparisons in Fig. S8 and Table S2 within the Supplementary Material [23], the giant  $\xi_{DL}^j$  for Pt/Hf multilayers can provide very compelling current and energy efficiencies for spin-torque applications, for instance for SOT-MRAMs, with a current efficiency superior to any other known material for practical applications.

The interesting peak behavior of  $\xi_{DL}^j$  at  $d \approx 0.6$  nm can be explained as being due to a competition between  $\rho_{xx}$  that increases quickly as a function of decreasing  $d$  [Fig. 2(b)] and the apparent spin Hall conductivity,  $\sigma_{SH}^* \equiv T_{int}\sigma_{SH} = (\hbar/2e)\xi_{DL}^j/\rho_{xx}$ , that decreases sharply as  $d$  decreases from 4 to 0.4 nm [Fig. 2(d)]. This decrease in  $\sigma_{SH}^*$  should be attributed partly to the enhanced attenuation

of spin current in the Hf insertion layers. The amorphous Hf has a short  $\lambda_s$  of approximately 1 nm and does not contribute to the generation of the spin current due to its negligible SHE [22]. Therefore, in the multilayers with small  $d$  where the total Hf thickness reaches  $>1$  nm, there should be a strong attenuation of the spin currents that diffuse to the FM interface from the bottom Pt layers to exert a SOT. In addition, the decrease of  $\sigma_{\text{SH}}^*$  with  $d$  could result in part from a strain-induced degradation of the Pt band structure (from a well-ordered fcc texture to a nearly amorphous structure, see Fig. S1). Nevertheless, in the Pt/Hf multilayers  $\sigma_{\text{SH}}^*$  is better preserved compared to that of uniformly doped Pt with Hf impurities. As shown in Fig. 2(d),  $\sigma_{\text{SH}}^*$  for the 4-nm  $\text{Pt}_{0.87}\text{Hf}_{0.13}$  is  $1.5 \times 10^5$  ( $\hbar/2e$ )  $\Omega^{-1} \text{m}^{-1}$  [19], which is a factor of 2 smaller than that of the Pt/Hf multilayers with similar Hf “concentration” (i.e., close to  $[\text{Pt}(1 \text{ nm})/\text{Hf}(0.2 \text{ nm})]_3/\text{Pt}(1 \text{ nm})$ ). This suggests that such HM multilayers with strong interfacial scattering can be generally advantageous over the corresponding impurity doping because in the latter  $\sigma_{\text{SH}}$  can be degraded more substantially by a stronger disturbance to the Pt band structure. We speculate that an enhancement of  $\xi_{\text{DL}}^j$  beyond the value of 0.37 that we obtain here should be possible if the increase of resistivity, the insertion layer attenuation of spin current, and the insertion-induced Pt strain can be better balanced, for instance, by using an insertion material that has a longer  $\lambda_s$  and an atomic radius closer to that of Pt (e.g., Ti) to minimize the disruption of the Pt crystal lattice and band structure.

### C. Spin-torque switching of magnetization

Now we show that our optimal Pt/Hf multilayer with strong interfacial scattering,  $[\text{Pt}(0.6 \text{ nm})/\text{Hf}(0.2 \text{ nm})]_5/\text{Pt}(0.6 \text{ nm})$ , is a particularly compelling spin Hall material for SOT research and technological applications. As the first example, we show the switching of a PMA Co layer ( $j_e = 1.7 \times 10^7 \text{ A/cm}^2$ , coercivity  $H_c = 0.43 \text{ kOe}$ ) enabled by the giant  $\xi_{\text{DL}}^j$  due to the SHE of the  $[\text{Pt}(0.6 \text{ nm})/\text{Hf}(0.2 \text{ nm})]_5/\text{Pt}(0.6 \text{ nm})$  multilayer (Fig. S4). As an independent check of the effectiveness of the enhancement of  $\xi_{\text{DL}}^j$  by Pt/Hf interfaces, we demonstrate antidamping switching of in-plane magnetized SOT-MRAM devices with  $\text{Fe}_{0.6}\text{Co}_{0.2}\text{B}_{0.2}$ -MgO MTJs. We fabricate two types of MRAM devices, devices A and B. Each MRAM device consists of a 300-nm-wide spin Hall channel of  $[\text{Pt}(0.6 \text{ nm})/\text{Hf}(0.2 \text{ nm})]_n/\text{Pt}(0.6 \text{ nm})$  ( $n = 5$  for device A and 6 for device B), an elliptical MTJ pillar of  $\text{Fe}_{0.6}\text{Co}_{0.2}\text{B}_{0.2}(1.6 \text{ nm})/\text{MgO}(1.6 \text{ nm})/\text{Fe}_{0.6}\text{Co}_{0.2}\text{B}_{0.2}(4 \text{ nm})$  ( $190 \times 45 \text{ nm}^2$  for device A or  $190 \times 74 \text{ nm}^2$  for device B), and protective capping layers of  $\text{Pt}(3 \text{ nm})/\text{Ru}(4 \text{ nm})$  (see the schematic in Fig. 3(a) and the cross-section STEM and EDS imaging results in Fig. S3). All devices are annealed at  $240^\circ\text{C}$ . For device B, 0.25-nm and 0.1-nm Hf spacers are inserted at the bottom and top of the 1.6-nm  $\text{Fe}_{0.6}\text{Co}_{0.2}\text{B}_{0.2}$  free

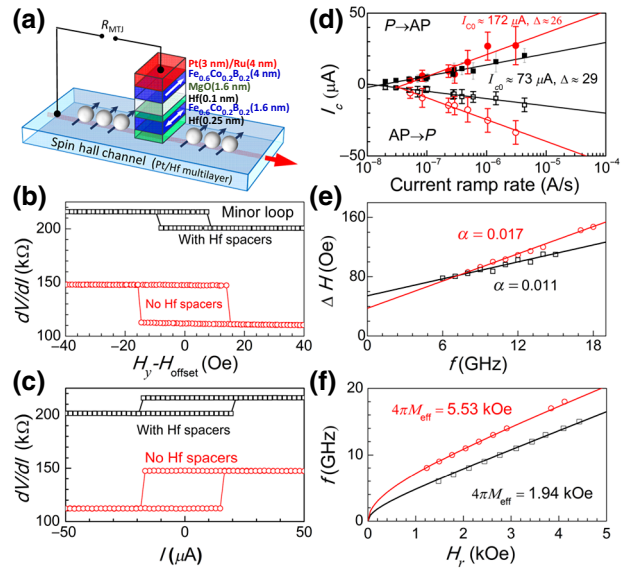


FIG. 3. (a) Schematic of the three-terminal MRAM device; (b) minor loop for switching by an in-plane applied magnetic field; (c) direct current switching loop; (d) critical current for  $P \rightarrow AP$  (solid) and  $AP \rightarrow P$  (open) switching as a function of current ramp rate; (e) FMR linewidth  $\Delta H$  as a function of the resonance frequency  $f$ ; (f) FMR resonance field  $H_r$  for the 1.6-nm  $\text{Fe}_{0.6}\text{Co}_{0.2}\text{B}_{0.2}$  magnetic free layers for device A (red) and device B (black). The solid lines in (d), (e), and (f) denote the best fits of data to Eq. (1),  $\Delta H = \Delta H_0 + (2\pi/\gamma)\alpha f$ , and  $f = (\gamma/2\pi)\sqrt{H_r(H_r + 4\pi M_{\text{eff}})}$ , respectively.  $\Delta H_0$  and  $\gamma$  are the inhomogeneous broadening of the FMR linewidth and the gyromagnetic ratio, respectively.

layer, respectively, to suppress the magnetic damping constant ( $\alpha$ ) [27] and reduce the effective magnetization ( $4\pi M_{\text{eff}}$ ), thereby reducing the critical current for antidamping switching [11]. The long axis of the elliptical MTJ pillars is along the  $y$  direction, transverse to the spin Hall channel and the write-current flow ( $x$  direction). In Figs. 3(b)–3(f), we compare the magnetization switching behaviors,  $\alpha$ , and  $4\pi M_{\text{eff}}$  of two representative MRAM devices without (device A, red) and with (device B, black) the two Hf spacers. Figure 3(b) shows the sharp switching minor loops of the MTJs under an in-plane magnetic field along the long axis of the MTJ pillar ( $H_y$ ). The minor loops are artificially centered after subtraction of the dipole fields ( $H_{\text{offset}} \approx 150 \text{ Oe}$  for device A and  $180 \text{ Oe}$  for device B) of the 4-nm  $\text{Fe}_{0.6}\text{Co}_{0.2}\text{B}_{0.2}$  reference layers.  $H_c$  of the free layer is 36 Oe for device A and 9 Oe for device B. The apparent tunnel magnetoresistance ratio (approximately 40% for devices A and approximately 7% for device B) is not very high, which is attributed to a large background resistance caused during the device fabrication process (i.e., the oxidization of the Ti adhesion layer between the MTJ pillars and the top Pt contact as indicated in Fig. S3).

Figure 3(c) shows the characteristic switching behavior of devices A and B as the write current in the spin Hall channel is ramped quasistatically (an in-plane field equal to  $H_{\text{offset}}$  is applied along the pillar long axis to compensate the dipole field from the reference layer). The MTJs show abrupt switching at write currents of 16  $\mu\text{A}$  for device A and 20  $\mu\text{A}$  for device B. Since thermal fluctuations assist the reversal of a nanoscale MTJ device during slow current ramps, we carry out ramp-rate measurements [Fig. 3(d)]. Within the macrospin model, the switching current  $I_c$  should scale with the ramp rate ( $\dot{I}$ ) following [28]

$$I_c = I_{c0} \left( 1 + \frac{1}{\Delta} \ln \frac{\tau_0 \Delta |\dot{I}|}{|I_{c0}|} \right). \quad (1)$$

Here  $I_{c0}$  is the critical switching current in the absence of thermal fluctuations,  $\Delta$  is the stability factor that represents the normalized magnetic energy barrier for reversal between the P and AP states, and  $\tau_0$  is the thermal attempt time, which we assume to be 1 ns. By fitting to Eq. (1), we obtain  $|I_{c0}| \approx 172 \pm 18 \mu\text{A}$  and  $\Delta \approx 26$  for device A and  $|I_{c0}| \approx 73 \pm 15 \mu\text{A}$  and  $\Delta \approx 29$  for device B after averaging the critical currents for P  $\rightarrow$  AP and AP  $\rightarrow$  P switching. The small critical switching currents are consistently reproduced by other devices. Considering a parallel resistor approximation, the current shunted into the Fe<sub>0.6</sub>Co<sub>0.2</sub>B<sub>0.2</sub> free layer and Hf spacers ( $\rho_{\text{Pt/Hf}} \approx 144 \mu\Omega \text{ cm}$ ,  $\rho_{\text{Fe}_{0.6}\text{Co}_{0.2}\text{B}_{0.2}} \approx \rho_{\text{Hf}} \approx 130 \mu\Omega \text{ cm}$ ) can be estimated to be approximately equal to  $0.2I_{c0}$  for both devices (see Fig. S6 and Table S1 within the Supplementary Material [23]). The critical switching density in the Pt spin Hall channel is therefore  $j_{c0} \approx (1.0 \pm 0.1) \times 10^7 \text{ A/cm}^2$  for device A (no Hf spacers) and  $j_{c0} \approx (3.6 \pm 0.7) \times 10^6 \text{ A/cm}^2$  for device B (with Hf spacers). Both the total critical switching and the low switching current density obtained from device B are much lower than those previously reported for in-plane [2, 10, 11, 20, 26] or perpendicular [12] spin-torque MTJs (see Table I).

According to the macrospin model,  $j_{c0}$  for antidamping torque switching of an in-plane magnetized MTJ is

given by  $j_{c0} = (2e/\hbar)\mu_0 M_s t \alpha (H_c + 4\pi M_{\text{eff}}/2)/\xi_{\text{DL}}^j$  [29]. With  $\alpha$  of 0.017 (0.011),  $4\pi M_{\text{eff}}$  of 5.54 (1.94) kOe, and  $M_s$  of 1240 emu/cm<sup>2</sup> for the magnetic free layer of device A (B) as calibrated from ferromagnetic resonance (FMR) [see Figs. 3(e) and 3(f)] and vibrating sample magnetometry measurements on unpatterned thin-film stacks, we estimate  $\xi_{\text{DL}}^j$  to be approximately 0.29 for device A and 0.17 for device B. The slight reduction of  $\xi_{\text{DL}}^j$  for device B compared to device A is mainly attributed to the spin-current attenuation due to the insertion of the 0.25-nm Hf layer in device B between the Pt/Hf multilayer and the Fe<sub>0.6</sub>Co<sub>0.2</sub>B<sub>0.2</sub> layer (spin diffusion length of Hf is approximately 1 nm [22]). Despite this reduction, this Hf spacer layer is still beneficial in that the suppression of  $\alpha$  and the reduction of  $4\pi M_{\text{eff}}$  for the free-layer interface more than compensates for the decrease in  $\xi_{\text{DL}}^j$ . The value of  $\xi_{\text{DL}}^j \sim 0.29$  for device A is significantly higher than those previously obtained in similar studies for MRAM devices based on  $\beta$ -W ( $\xi_{\text{DL}}^j = -0.15$ ) [11], Pt<sub>0.85</sub>Hf<sub>0.15</sub> ( $\xi_{\text{DL}}^j = 0.098$ ) [20], and Pt ( $\xi_{\text{DL}}^j = 0.12$ ) [27]. We do note that  $\xi_{\text{DL}}^j = 0.29$  from the MRAM ramp-rate experiment is approximately 20% less than the value determined from harmonic response measurements [see Fig. 2(c)]. This difference may be partly attributed to an increased magnetic damping of nanoscale devices compared to thin-film stacks due to, e.g., the ion-beam damage and the side-wall oxidation of the nanopillar during the device fabrication process. Tapering of the free layer, which is formed during the ion milling process due to the resist shielding effect (see more details in Fig. S3), can significantly increase the effective volume of the free layer of the MRAM device and lead to additional current shunting into the free layer. This current shunting into the tapering area is not taken into account in our calculation. For the same reasons,  $\xi_{\text{DL}}^j$  of spin Hall materials is generally found to be underestimated in the ramp-rate results of other nanoscale MRAM devices compared to those in direct SOT measurements on microscale Hall bars [10, 11, 20] (e.g., for W,  $\xi_{\text{DL}}^j$  is approximately 0.15 from MRAM ramp-rate measurements and approximately 0.20 from bilayer spin-torque measurements [11]).

TABLE I. Comparison of SOT-MRAM devices. Both the critical switching current ( $I_c$ ) and the critical switching current density ( $j_{c0}$ ) for our Pt/Hf multilayer device are the lowest among all spin Hall materials demonstrated in room-temperature SOT-MRAM devices. Here  $[\text{Pt}/\text{Hf}]_n$  represents the multilayers of  $[\text{Pt}(0.6 \text{ nm})/\text{Hf}(0.2 \text{ nm})]_6/\text{Pt}(0.6 \text{ nm})$ .

Materials	SOT device	$I_{c0}$ (mA)	$j_{c0}$ (MA/cm <sup>2</sup> )	Refs.
$[\text{Pt}/\text{Hf}]_n$	In-plane MTJ	0.073	3.6	This work
W	In-plane MTJ	0.15	5.4	[11]
W	In-plane MTJ	0.95	18	[26]
Pt	In-plane MTJ	0.67	40	[10]
Ta	In-plane MTJ	2.0	32	[3]
Pt <sub>0.85</sub> Hf <sub>0.15</sub>	In-plane MTJ	0.56	14	[20]
Ta	PMA MTJ	>20	>50	[12]

We point out that the record-low critical switching current (current density) of the SOT-MRAMs based on Pt/Hf multilayers is a technologically interesting achievement. The three-terminal SOT-MRAM is an advantageous current- and energy-efficient cache-memory candidate because the separation of the read and write channels in the three-terminal geometry offers additional advantages over the conventional two-terminal spin-transfer-torque geometry, e.g., unlimited endurance, faster write (sub-nanosecond [11]), faster readout without read disturbance, lower write energy, and an allowance for a thick MgO barrier for enhanced tunnel magnetoresistance ratio.

### III. CONCLUSION

In conclusion, we demonstrate, from direct spin-torque measurements and also spin-torque switching experiments of magnetic layers with both perpendicular and in-plane magnetic anisotropy, that introducing additional interface electron scattering within Pt by inserting submonolayer layers of Hf can significantly increase  $\xi_{\text{DL}}^j$ . For example, we show an increase of  $\xi_{\text{DL}}^j$  from  $0.17 \pm 0.01$  for a simple 4-nm-thick single Pt layer to  $0.37 \pm 0.01$  for a [Pt(0.6 nm)/Hf(0.2 nm)]<sub>7</sub>/Pt(0.6 nm) multilayer despite the attenuation of spin current from Pt by the Hf insertion layers. Taking advantage of this interface-scattering-enhanced spin Hall ratio in the Pt/Hf multilayers, we demonstrate deterministic switching of IMA MRAM devices with a zero-temperature critical switching current of approximately  $73 \mu\text{A}$  and a critical switching current density of approximately  $3.6 \times 10^6 \text{ A/cm}^2$ , both of which are much lower than the previously reported results. Our optimized multilayer, [Pt(0.6 nm)/Hf(0.2 nm)]<sub>5</sub>/Pt(0.6 nm) (with  $\xi_{\text{DL}}^j = 0.37$ ,  $\rho_{xx} = 144 \mu\Omega \text{ cm}$ ), represents a highly efficient generator of spin-orbit torque that is also compatible with integration technology (e.g., allowing easy growth with standard sputtering techniques on Si substrates) for development of low-power magnetic memories, oscillators, and logic. Our findings also provide an alternative strategy with the potential to magnify SOTs generated by other heavy metals, e.g., the low-resistivity Pd-Pt [17] or Au-Pt [18].

### ACKNOWLEDGMENTS

This work was supported in part by the Office of Naval Research (Grant No. N00014-15-1-2449), by the NSF MRSEC program (Grant No. DMR-1719875) through the Cornell Center for Materials Research, and by the Office of the Director of National Intelligence (ODNI), Intelligence Advanced Research Projects Activity (IARPA), via contract No. W911NF-14-C0089. The views and conclusions contained herein are those of the authors and should not be interpreted as necessarily representing the official policies or endorsements, either expressed or implied, of the ODNI,

IARPA, or the U.S. Government. The U.S. Government is authorized to reproduce and distribute reprints for Governmental purposes notwithstanding any copyright annotation thereon. The devices were fabricated in part at the Cornell NanoScale Facility, an NNCI member supported by NSF Grant No. ECCS-1542081. The TEM measurements performed at Shaanxi Normal University and Beijing University of Technology were supported by the Science and Technology Program of Shaanxi Province (Grant No. 2019JQ-433) and the Fundamental Research Funds for the Central Universities (Grant No. GK201903024).

- [1] I. M. Miron, K. Garello, G. Gaudin, P.-J. Zermatten, M. V. Costache, S. Auffret, S. Bandiera, B. Rodmacq, A. Schuhl, and P. Gambardella, Perpendicular switching of a single ferromagnetic layer induced by in-plane current injection, *Nature* **476**, 189 (2011).
- [2] C. O. Avci, A. Quindeau, C.-F. Pai, M. Mann, L. Caretta, A. S. Tang, M. C. Onbasli, C. A. Ross, and G. S. D. Beach, Current-induced switching in a magnetic insulator, *Nat. Mater.* **16**, 309 (2017).
- [3] L. Liu, C.-F. Pai, Y. Li, H. W. Tseng, D. C. Ralph, and R. A. Buhrman, Spin-torque switching with the giant spin Hall effect of tantalum, *Science* **336**, 555 (2012).
- [4] G. Yu, P. Upadhyaya, Y. Fan, J. G. Alzate, W. Jiang, K. L. Wong, S. Takei, S. A. Bender, L.-T. Chang, Y. Jiang, M. Lang, J. Tang, Y. Wang, Y. Tserkovnyak, P. K. Amiri, and K. L. Wang, Switching of perpendicular magnetization by spin-orbit torques in the absence of external magnetic fields, *Nat. Nanotechnol.* **9**, 548 (2014).
- [5] V. E. Demidov, S. Urazhdin, H. Ulrichs, V. Tiberkevich, A. Slavin, D. Baither, G. Schmitz, and S. O. Demokritov, Magnetic nano-oscillator driven by pure spin current, *Nat. Mater.* **11**, 1028 (2012).
- [6] P. P. J. Haazen, E. Muré, J. H. Franken, R. Lavrijsen, H. J. M. Swagten, and B. Koopmans, Domain wall depinning governed by the spin Hall effect, *Nat. Mater.* **12**, 299 (2013).
- [7] W. Jiang, P. Upadhyaya, W. Zhang, G. Yu, M. B. Jungfleisch, F. Y. Fradin, J. E. Pearson, Y. Tserkovnyak, K. L. Wang, O. Heinonen, S. G. E. Velthuis, and A. Hoffmann, Blowing magnetic skyrmion bubbles, *Science* **349**, 283 (2015).
- [8] O. J. Lee, L. Q. Liu, C. F. Pai, Y. Li, H. W. Tseng, P. G. Gowtham, J. P. Park, D. C. Ralph, and R. A. Buhrman, Central role of domain wall depinning for perpendicular magnetization switching driven by spin torque from the spin Hall effect, *Phys. Rev. B* **89**, 024418 (2014).
- [9] L. Zhu, D. C. Ralph, and R. A. Buhrman, Spin-Orbit Torques in Heavy-Metal-Ferromagnet Bilayers With Varying Strengths of Interfacial Spin-Orbit Coupling, *Phys. Rev. Lett.* **122**, 077201 (2019).
- [10] S. V. Aradhya, G. E. Rowlands, J. Oh, D. C. Ralph, and R. A. Buhrman, Nanosecond-timescale low energy switching of in-plane magnetic tunnel junctions through dynamic Oersted-field-assisted spin Hall effect, *Nano. Lett.* **16**, 5987 (2016).

- [11] S. Shi, Y. Ou, S. V. Aradhya, D. C. Ralph, and R. A. Buhrman, Fast, Low-Current Spin-Orbit Torque Switching of Magnetic Tunnel Junctions Through Atomic Modifications of the Free Layer Interfaces, *Phys. Rev. Applied* **9**, 011002 (2018).
- [12] M. Cubukcu, O. Boulle, N. Mikuszeit, C. Hamelin, T. Brächer, N. Lamard, M.-C. Cyrille, L. Buda-Prejbeanu, K. Garello, I. Mihai Miron, O. Klein, G. de Loubens, V. V. Naletov, J. Langer, B. Ocker, P. Gambardella, and G. Gaudin, Ultra-fast perpendicular spin-orbit torque MRAM, *IEEE Trans. Magn.* **54**, 9300204 (2018).
- [13] S. Fukami, T. Anekawa, C. Zhang, and H. Ohno, A spin-orbit torque switching scheme with collinear magnetic easy axis and current configuration, *Nat. Nanotechnol.* **11**, 621 (2016).
- [14] T. Tanaka, H. Kontani, M. Naito, T. Naito, D. S. Hirashima, K. Yamada, and J. Inoue, Intrinsic spin Hall effect and orbital Hall effect in 4d and 5d transition metals, *Phys. Rev. B* **77**, 165117 (2008).
- [15] G. Y. Guo, S. Murakami, T.-W. Chen, and N. Nagaosa, Intrinsic Spin Hall Effect in Platinum: First-Principles Calculations, *Phys. Rev. Lett.* **100**, 096401 (2008).
- [16] L. Liu, T. Moriyama, D. C. Ralph, and R. A. Buhrman, Spin-Torque Ferromagnetic Resonance Induced by the Spin Hall Effect, *Phys. Rev. Lett.* **106**, 036601 (2011).
- [17] L. J. Zhu, K. Sobotkiewich, X. Ma, X. Li, D. C. Ralph, and R. A. Buhrman, Strong damping-like spin-orbit torque and tunable Dzyaloshinskii-Moriya interaction generated by low-resistivity  $Pd_{1-x}Pt_x$  alloys, *Adv. Funct. Mater.* **29**, 1805822 (2019).
- [18] L. Zhu, D. C. Ralph, and R. A. Buhrman, Efficient Spin Current Generation by the Spin Hall Effect in  $Au_{1-x}Pt_x$ , *Phys. Rev. Applied* **10**, 031001 (2018).
- [19] M.-H. Nguyen, M. Zhao, D. C. Ralph, and R. A. Buhrman, Enhanced spin Hall torque efficiency in  $Pt_{100-x}Al_x$  and  $Pt_{100-x}Hf_x$  alloys arising from the intrinsic spin Hall effect, *Appl. Phys. Lett.* **108**, 242407 (2016).
- [20] M.-H. Nguyen, S. Shi, G. E. Rowlands, S. V. Aradhya, C. L. Jermain, D. C. Ralph, and R. A. Buhrman, Efficient switching of 3-terminal magnetic tunnel junctions by the giant spin Hall effect of  $Pt_{85}Hf_{15}$  alloy, *Appl. Phys. Lett.* **112**, 062404 (2016).
- [21] J. W. Lee, Y.-W. Oh, S.-Y. Park, A. I. Figueroa, G. van der Laan, G. Go, K.-J. Lee, and B.-G. Park, Enhanced spin-orbit torque by engineering Pt resistivity in Pt/Co/AlO<sub>x</sub> structures, *Phys. Rev. B* **96**, 064405 (2017).
- [22] Y. Ou, C.-F. Pai, S. Shi, D. C. Ralph, and R. A. Buhrman, Origin of fieldlike spin-orbit torques in heavy metal/ferromagnet/oxide thin film heterostructures, *Phys. Rev. B* **94**, 140414(R) (2016).
- [23] See Supplementary Material at <http://link.aps.org/supplemental/10.1103/PhysRevApplied.11.061004> for more details on experimental methods, structural characterization of Pt/Hf multilayers, cross-section STEM and EDS imaging of a MRAM device, harmonic response measurements, current-induced switching of a perpendicular Co layer, estimation of current shunting into the MTJ free layer, current switching and ramp-rate experiments, and write energy and current for SOT-MRAM devices based on different strong spin Hall metals.
- [24] J. Kim, J. Sinha, M. Hayashi, M. Yamanouchi, S. Fukami, T. Suzuki, S. Mitani, and H. Ohno, Layer thickness dependence of the current-induced effective field vector in Ta|CoFeB|MgO, *Nat. Mater.* **12**, 240 (2013).
- [25] C. O. Avci, K. Garello, M. Gabureac, A. Ghosh, A. Fuhrer, S. F. Alvarado, and P. Gambardella, Interplay of spin-orbit torque and thermoelectric effects in ferromagnet/normal-metal bilayers, *Phys. Rev. B* **90**, 224427 (2014).
- [26] C.-F. Pai, L. Liu, Y. Li, H. W. Tseng, D. C. Ralph, and R. A. Buhrman, Spin transfer torque devices utilizing the giant spin Hall effect of tungsten, *Appl. Phys. Lett.* **101**, 122404 (2012).
- [27] M.-H. Nguyen, C.-F. Pai, K. X. Nguyen, D. A. Muller, D. C. Ralph, and R. A. Buhrman, Enhancement of the anti-damping spin torque efficacy of platinum by interface modification, *Appl. Phys. Lett.* **106**, 222402 (2015).
- [28] E. B. Myers, F. J. Albert, J. C. Sankey, E. Bonet, R. A. Buhrman, and D. C. Ralph, Thermally Activated Magnetic Reversal Induced by a Spin-Polarized Current, *Phys. Rev. Lett.* **89**, 196801 (2002).
- [29] J. Z. Sun, Spin-current interaction with a monodomain magnetic body: A model study, *Phys. Rev. B* **62**, 570 (2000).